Magn Reson Mater Phy (2016) 29:751–763
DOI 10.1007/s10334-016-0540-9

RESEARCH ARTICLE

Intravoxel incoherent motion analysis of abdominal organs: computation of reference parameters in a large cohort of C57Bl/6 mice and correlation to microvessel density

Christian Eberhardt[1] · Moritz C. Wurnig[1] · Andrea Wirsching[2] · Cristina Rossi[1] · Markus Rottmar[1,3] · Pinar S. Özbay[1,4] · Lukas Filli[1] · Mickael Lesurtel[5] · Andreas Boss[1]

Received: 5 February 2015 / Revised: 19 February 2016 / Accepted: 22 February 2016 / Published online: 19 April 2016

Abstract
Objective Diffusion-weighted magnetic resonance imaging (DW-MRI) combined with intravoxel incoherent motion (IVIM) analysis may be applied for assessment of organ lesions, diffuse parenchymal pathologies, and therapy monitoring. The aim of this study was to determine IVIM reference parameters of abdominal organs for translational research in a large cohort of C57Bl/6 laboratory mice.
Materials and methods Anesthetized mice ($n = 29$) were measured in a 4.7 T small-animal MR scanner with a diffusion-weighted echo-planar imaging sequence at the *b*-values 0, 13, 24, 55, 107, 260, 514, 767, 1020 s/mm^2. IVIM analysis was conducted on the liver, spleen, renal medulla and cortex, pancreas, and small bowel with computation of the true tissue diffusion coefficient D_t, the perfusion fraction f_p, and the pseudodiffusion coefficient D_p. Microvessel density (MVD) was assessed by immunohistochemistry (IHC) against panendothelial cell antigen CD31.
Results Mean values of the different organs [D_t (10^{-3} mm^2/s); f_p (%); D_p (10^{-3} mm^2/s); MVD (MV/mm^2)]: liver 1.15 ± 0.14; 14.77 ± 6.15; 50.28 ± 33.21, 2008.48 ± 419.43, spleen 0.55 ± 0.12; 9.89 ± 5.69; 24.46 ± 17.31; n.d., renal medulla 1.50 ± 0.20; 14.63 ± 4.07; 35.50 ± 18.01; 1231.88 ± 290.61, renal cortex 1.34 ± 0.18; 10.83 ± 3.70; 16.74 ± 6.74; 810.09 ± 193.50, pancreas 1.23 ± 0.22; 20.12 ± 7.46; 29.35 ± 17.82, 591.15 ± 86.25 and small bowel 1.06 ± 0.13; 16.48 ± 3.63; 15.31 ± 7.00; 420.50 ± 168.42. Unlike D_t and f_p, D_p correlates significantly with MVD ($r = 0.90$, $p = 0.037$).
Conclusion This systematic evaluation of murine abdominal organs with IVIM and MVD analysis allowed to establish reference parameters for future DW-MRI translational research studies on small-animal disease models.

✉ Christian Eberhardt
christian.eberhardt@usz.ch

Moritz C. Wurnig
moritz.wurnig@usz.ch

Andrea Wirsching
andrea.wirsching@usz.ch

Cristina Rossi
cristina.rossi@usz.ch

Markus Rottmar
markus.rottmar@empa.ch

Pinar S. Özbay
pinar.oezbay@usz.ch

Lukas Filli
lukas.filli@usz.ch

Mickael Lesurtel
mickael.lesurtel@usz.ch

Andreas Boss
andreas.boss@usz.ch

[1] Department of Diagnostic and Interventional Radiology, University Hospital Zurich, Raemistrasse 100, 8091 Zurich, Switzerland

[2] Department of Visceral and Transplant Surgery, University Hospital Zurich, Raemistrasse 100, 8091 Zurich, Switzerland

[3] Laboratory for Biointerfaces, Empa, Swiss Federal Laboratories for Materials Science and Technology, Lerchenfeldstrasse 5, 9014 St. Gallen, Switzerland

[4] Institute for Biomedical Engineering, University of Zurich and ETH Zurich, Gloriastrasse 35, 8092 Zurich, Switzerland

[5] Swiss HPB and Transplant Center, University Hospital Zurich, Rämistrasse 100, 8091 Zurich, Switzerland

Keywords Diffusion-weighted magnetic resonance imaging · Echo-planar imaging · Intravoxel incoherent motion · IVIM · Pseudodiffusion · Microvessel density · Microvessel count

Introduction

In recent years, diffusion-weighted magnetic resonance imaging (DW-MRI) has been widely implemented as a supplementary routine sequence to clinical MRI protocols, providing additional diagnostic value for detection and characterization of focal lesions in the abdomen [1–4]. Malignant tumors are often characterized by restricted molecular water diffusion due to their higher degree of cellularity. Applying DW-MRI, neoplastic pathologies thus exhibit diminished signal attenuation compared with healthy tissue. The degree of water diffusion is usually described by the apparent diffusion coefficient (ADC), assuming monoexponential signal decay in dependence of the *b*-value, a value describing the DW strength of the MR sequence. Typically, the ADC is determined by fitting obtained signal intensities to the equation:

$$S_b/S_0 = \exp(-b \cdot \mathrm{ADC}), \quad (1)$$

where S_b corresponds to signal intensities over a series of *b*-values and S_0 to signal intensity without DW.

However, this equation does not entirely mirror the true nature of water motility in parenchyma, as measurements at low *b*-values are influenced by rapid water motion in tissue microcapillaries due to perfusion effects. To account for these fast-moving water spins, the model of intravoxel incoherent motion (IVIM) has been proposed [5, 6]. This approach allows to disentangle and to quantify the overlapping driving forces of water motion within tissues, diffusion, and perfusion via bi-exponential fitting of measured signal intensities versus *b*-values. Perfusion-related water motility due to directed microcirculation within a randomly oriented capillary system, termed pseudodiffusion, can only be measured at low *b*-values, as the signal contribution from fast-moving spins dephases and approximates 0 at higher *b*-values ($b \geq$ 100–200 s/mm^2). In contrast, the signal contribution by purely thermally driven diffusion is present in all measurements at *b*-values >0. Although sparsely applied to abdominal organs initially after its introduction [7, 8], the IVIM concept gained increasing importance in clinical research on the abdomen, and many IVIM studies in humans have been carried out to identify and characterize organ lesions and monitor therapy of liver [9–14], kidney [15–17], and pancreas [18, 19].

The laboratory mouse is a commonly used animal model for researching a variety of disorders and diseases and occasionally IVIM has been adopted for translational research purposes [20–22]. One investigation using a tumor mouse model reported a significant correlation of microvessel density (MVD) with perfusion-related IVIM parameters and suggested the applicability of IVIM measurements for noninvasive MVD evaluation [20]. However, a systematic and comprehensive assessment of IVIM parameters on the mouse abdomen has not yet been performed. This paper reports the obtained true tissue diffusion coefficient D_t, pseudodiffusion coefficient D_p, and the perfusion fraction f_p of healthy liver, spleen, renal medulla and cortex, pancreas and small bowel of a large cohort MRI study on C57Bl/6 mice as reference for future murine translational research. Additionally, obtained IVIM parameters were correlated to the MVD as morphological tissue parameter. Furthermore, this study provides a suitable measurement protocol for DW-MRI implemented in a small-animal MR scanner and the corresponding postprocessing routines for IVIM analysis of murine abdominal organs.

Materials and methods

Imaging protocol

The study on C57Bl/6 mice was approved by the local veterinary committee (license no. 131/2011). Mice (n = 29; 25–32 g) aged 8–10 weeks were placed in the prone position on a respiratory sensor (SA Instruments, Stony Brook, NY, USA) located in a plastic holder with nose cone, providing air supplemented with 1.0–1.5 % isoflurane, and covered by a warming pad to maintain body temperature. Experiments were performed on a 4.7 T small-animal MRI system (Pharmascan 47/16 US; Bruker BioSpin MRI GmbH, Ettlingen, Germany) with a gradient strength of 375 mT/m and a slew rate of 3375 T/m/s equipped with a linear polarized hydrogen whole-body mouse transmit–receive radiofrequency coil. After a gradient-echo localizer scan in three spatial directions, a respiratory-triggered DW spin-echo echo-planar imaging sequence covering the abdomen with ten axial slices, each with a 1.5-mm slice thickness was applied with the following settings: effective TE = 30 ms, TR = 3000 ms, number of signal averages = 8, fat suppression prepulse, field of view (FoV) 30 × 30 mm, acquisition matrix 128 × 128, voxel (vx) size 0.234 mm × 0.234 mm × 1.5 mm. Nine different *b*-values were acquired with 0, 13, 24, 55, 107, 260, 514, 767, 1020 s/mm^2. The calculated acquisition time of this sequence was 14:22 min; due to the respiratory-triggered acquisition, the actual scan duration amounted to ~20 min.

Defining a region of interest (ROI)

Image quality of the DW abdominal data sets of C57Bl/6 mice ($n = 29$) was visually assessed, and individual slices of a mouse data set affected by either deleterious respiratory or peristaltic motion artifacts were excluded from further analysis. The remaining number of axial sections with suitable image quality contributed to IVIM analysis of the abdominal organs and allowed computation of organ-specific IVIM diffusion parameters of the liver ($n = 21$), spleen ($n = 14$), renal cortex and medulla ($n = 20$), pancreas ($n = 18$), and small bowel ($n = 15$). Furthermore, signal-to-noise ratio (SNR) was estimated using the following equation: $\mathrm{SNR} = \mathrm{S_{liver}}/\mathrm{SD_{background}}$ with S_{liver} meaning signal intensity of liver parenchyma and $SD_{\mathrm{background}}$ the standard deviation (SD) of the background signal.

Applying custom-written Matlab scripts (MathWorks, Natick, MA, USA), a region of interest (ROI) analysis was performed to quantify signal intensity for each *b*-value and to subsequently extract IVIM-specific diffusion parameters of the fitted bi-exponential signal intensity curve as a function of the *b*-values. Three independent polygonal ROIs were defined on one slice of the proton-density-weighted image acquired at $b = 0$ s/mm^2 of each of the following abdominal organs/organ compartments: liver, spleen, renal cortex and medulla, pancreas, and small bowel and then transferred onto the subsequent *b*-value images of the same data set. The obtained signal-intensity curves were normalized to 1 using the S_0 value obtained for the ROI on the $b = 0$ s/mm^2 image. For the liver, ROIs were drawn in the right lobe under avoidance of large vessel structures and for the spleen into the periphery under avoidance of the fibrous capsule; representative ROIs are shown in Fig. 1. The assessed ROIs had the following sizes: liver 41.3 ± 18.6 vx; kidney medulla 22.0 ± 5.5 vx; kidney cortex 20.4 ± 5.2 vx; spleen 18.4 ± 4.0 vx; pancreas 26.8 ± 14.1 vx; bowel 24.4 ± 6.4 vx. Image noise was determined in an ROI positioned outside the body in the upper left hand corner in the background of the image and corrected by squared subtraction according to Gudbjartsson [23].

IVIM image analysis

Besides the rather slow molecular diffusion, foremost pseudodiffusion, the perfusion-related faster water motility in the microcapillary network contributes significantly to the retrieved signal attenuation for measurements at small *b*-values. The IVIM concept describes both contributing effects to water motility in tissues by a bi-exponential relationship between *b*-value and measured signal intensity:

$$S_b/S_0 = f_p \cdot \exp(-b \cdot D_p) + (1 - f_p) \cdot \exp(-b \cdot D_t) \quad (2)$$

Thereby, D_p represents the pseudodiffusion coefficient, f_p represents the relative fraction of perfusion-related water motility, and D_t represents the true tissue diffusion coefficient. As the impact of pseudodiffusion on signal attenuation decreases with increasing *b*-value, these IVIM parameters can be determined by a stepwise IVIM analysis, thus providing higher stability compared with a direct bi-exponential fit of all three parameters [24]. Here, the pseudodiffusion term was expected to be small and negligible for $b \geq 100$ s/mm^2, and hence Eq. (2) could be simplified to a monoexponential correlation [5]:

$$S_b/S_0 = (1 - f_p) \cdot \exp(-b \cdot D_t) \quad (3)$$

Initially, the tissue diffusion coefficient D_t and perfusion fraction f_p were inferred by a linear fit to the log-transformed signal intensities; subsequently, the pseudodiffusion coefficient D_t could be retrieved by a bi-exponential fit to all signal intensities with set predetermined f_p and D_t.

The stepwise algorithm is described as follows:

1. For the log-transformed signal intensities of high *b*-values, D_t is represented by the slope of the linear least-square-fitted regression line, S_0' with $S_0' = S_0(1 - f_p)$ being the *y*-axis intercept of the regression line:

$$\log S_b = -D_t \cdot b + \log S_0' \quad (4)$$

2. The perfusion fraction f_p can be deduced by S_0, the measured signal intensity within the ROI on the b_0-image and the calculated S_0':

$$f_p = \frac{S_0 - S_0'}{S_0} \quad (5)$$

3. Finally, the pseudodiffusion coefficient D_p is determined by a bi-exponential fit to the signal intensities of all *b*-values based on Eq. (2) using the Levenberg–Marquardt algorithm with preset f_p and D_t values.

Immunohistochemistry (IHC) and MVD determination

To further assess the MVD, the corresponding abdominal organs were extracted from three mice (27–29 g; 9 weeks). The tissue specimens were fixed in 4 % formalin (24 h, 20 °C), dehydrated through a series of graded alcohols, cleared in Histo Clear (Brunschwig, Basel, Switzerland), and impregnated with liquid wax (Paraplast, Leica Biosystems, Muttenz, Switzerland). Larger tissue blocks were then cut into ~3- to 5-mm-thick sections along the transversal plane and embedded in paraffin. Of each animal and organ, three tissue sections (3 µm) at three different levels, each at 30-µm distance, were cut in transversal orientation as displayed on the corresponding IVIM-assessed DW-MRIs and mounted on positively charged microscope slides. For IHC, sections

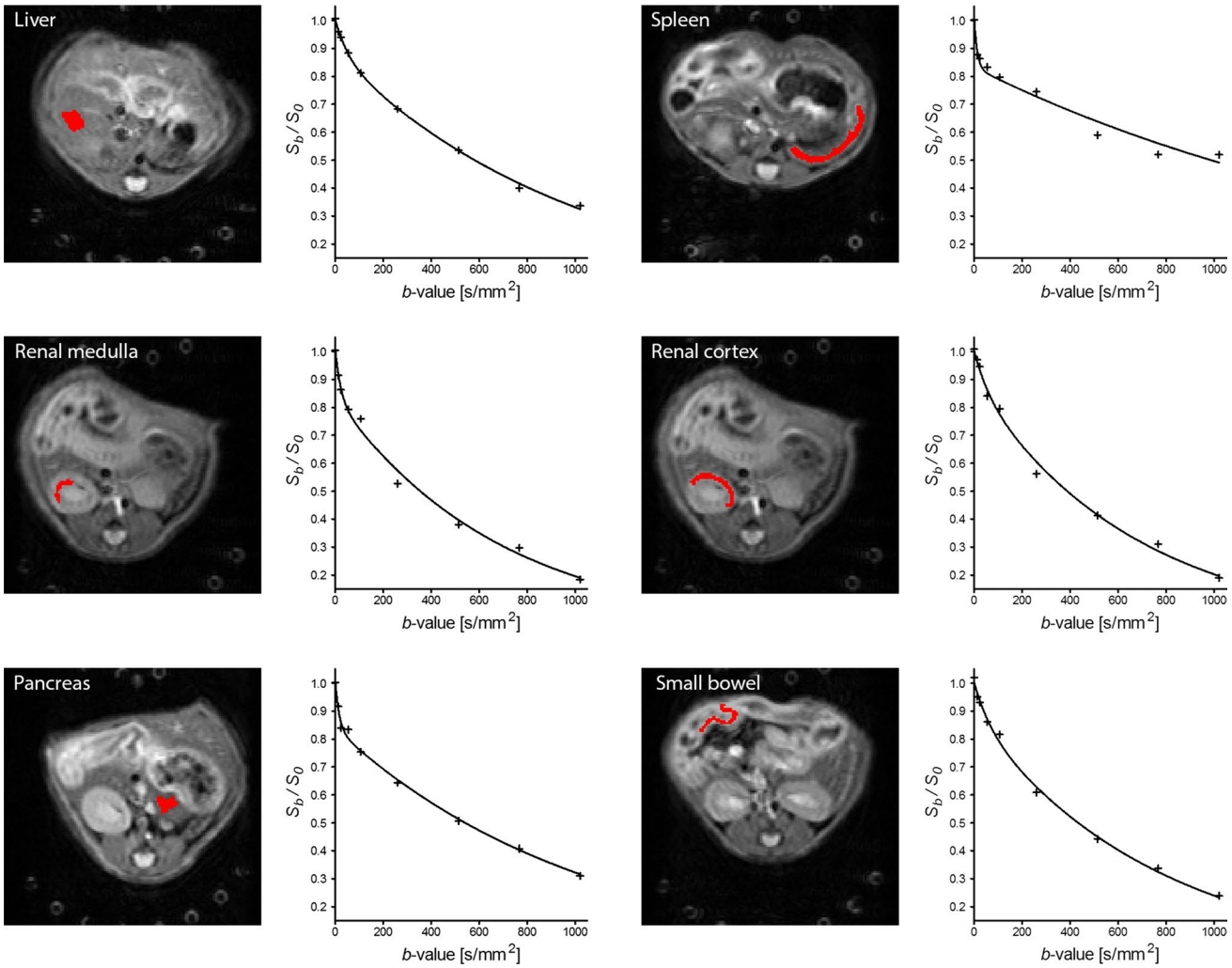

Fig. 1 Representative regions of interest drawn on the respective axial, non-diffusion-weighted image ($b = 0$ s/mm^2) within the liver, spleen, renal medulla, renal cortex, pancreas, and small bowel. The diagram on the *right of each image* depicts the retrieved relative signal intensities at nine different *b*-values (0, 13, 24, 55, 107, 260, 514, 767, 1020 mm^2/s) of the assessed organs and the accordingly fitted bi-exponential signal attenuation curve using the outlined IVIM model

were transferred to Target Retrieval Solution High pH (K8004, Dako Denmark A/S, Glostrup, Denmark, 20 min, 97 °C) within a Dako PT Link (PT100/PT101, Dako Denmark A/S) for the three-in-one procedure, i.e., deparaffinization, rehydration, and heat-induced epitope retrieval (HIER) of formalin-fixed, paraffin-embedded tissue sections. A standard IHC staining protocol was performed on a Dako Autostainer Link48 Instrument (Dako Denmark A/S) for the panendothelial cell marker CD31 using a polyclonal rabbit anti-CD31 immunoglobulin G (IgG) (AB28364, Abcam, Cambridge, UK) working dilution 1:50 in Dako Antibody Diluent (S2022, Dako Denmark A/S, 20 min, 20 °C). The visualization system consisted of the Dako EnVision™ Rabbit/HRP/DAB and hematoxylin as counterstain. After IHC staining, tissue specimens were dehydrated, permanently mounted, and microscopically evaluated.

The number of CD31-positive cells, i.e., the MVD was determined by manual counting of MVs within five random fields of view per tissue section (FoV 0.069 mm^2) using ImageJ (http://imagej.nih.gov/) [25] after minor contrast/brightness adjustments for better visibility of the immunoreactive cells on images acquired in bright-field (BF) mode (400× magnification) on a Nikon Eclipse Ti fluorescence microscope (Amsterdam, The Netherlands). Single immunoreactive endothelial cells spatially isolated and distinct from other MVs in their vicinity were counted as MVs. Moreover, the density of proximal convoluted tubules (PCT) and distal convoluted tubules (DCT) of the renal cortex was determined as outlined for the MVD.

Statistical evaluation

For descriptive analysis, mean values, SDs, as well as 95 % confidence intervals (CIs) of IVIM parameters were calculated, and numeric data are presented as the mean ± SD. Statistical evaluation of IVIM parameters between different organs was performed with analysis of variance (ANOVA) with Bonferroni correction using Prism 5 software (GraphPad Software, Inc., La Jolla, CA, USA); CIs were computed with bias-corrected accelerated bootstrapping analysis based on 10,000 bootstrap samples using SPSS Software vers. 22 (IBM Corporation, Armonk, NY, USA). The correlation of MVD and IVIM parameters was assessed using Spearman's rank correlation with SPSS software. All p values <0.05 were considered statistically significant.

Results

The SNR was determined on images obtained for the liver with SNR >100 (120.28 ± 17.32). Examples of representative ROIs drawn on axial non-diffusion-weighted images ($b = 0$ s/mm^2) of the liver, spleen, renal cortex and medulla, pancreas and small bowel, together with the obtained relative signal intensities for each b-value and the fitted bi-exponential signal attenuation curves, are illustrated in Fig. 1. The scatter plots in Fig. 2 depict each individual value determined for the true tissue diffusion coefficient D_t, pseudodiffusion coefficient D_p, and perfusion fraction f_p, as well as the calculated mean of IVIM diffusion parameters D_t, D_p and f_p, obtained for each assessed organ; statistical significance is indicated by asterisks. Mean values of these IVIM parameters together with their SD and CI after bootstrapping analysis for each investigated abdominal organ are provided as a comprehensive summary in Table 1. Furthermore, Table 1 provides the MVD as retrieved by counting the MVs and, again, also for MVD CI after bootstrapping analysis.

As shown in Fig. 1 especially, the signal attenuation curves retrieved for the spleen and pancreas, less pronounced for the renal medulla, display the characteristic bi-exponential curvature with an initially strong signal loss at lower b-values related to pseudodiffusion and then following, a diminished, attenuated signal decline at higher b-values attributed to true tissue diffusion. For the spleen, this distinctive bi-exponential pattern is attributed to the lowest true tissue diffusion coefficient D_t, hence highest diffusion hindrance, of all assessed abdominal organs in conjunction with perfusion-related parameters D_p and f_p comparable to other investigated tissues (Table 1). In contrast, the pancreas has the highest perfusion fraction f_p of all evaluated organs, determining this prominent bi-exponential

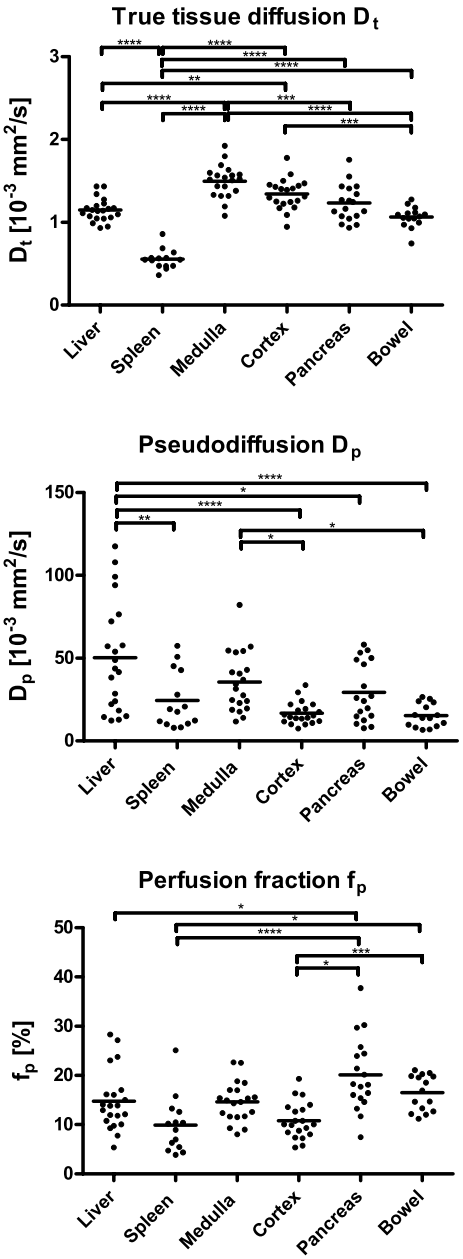

Fig. 2 True tissue diffusion coefficient D_t, pseudodiffusion coefficient D_p, and perfusion fraction f_p, as well as the calculated mean of diffusion parameters D_t, D_p, and f_p obtained for each assessed abdominal organ. Statistical significance was assessed by Bonferroni corrected ANOVA test and is indicated by asterisks (*$p \leq 0.05$; **$p \leq 0.01$; ***$p \leq 0.001$; ****$p \leq 0.0001$)

curvature, whereas the true tissue diffusion coefficient D_t and the pseudodiffusion coefficient D_p are similar to the other examined tissues (Table 1).

The obtained mean IVIM parameters are organ and compartment specific (Table 1). The determined mean true tissue diffusion coefficient D_t was highest in the renal medulla, at $D_t = 1.50 \times 10^{-3}$ mm^2/s, followed by the renal cortex at $1.34 \pm 0.18 \times 10^{-3}$ mm^2/s, then pancreas

Table 1 Mean ± standard deviation (SD) and confidence interval (CI) after bootstrapping analysis of the true tissue diffusion coefficient D_t, pseudodiffusion coefficient D_p, perfusion fraction f_p, and MVD of the assessed abdominal organs

	D_t (10^{-3} mm^2/s)	CI 95 % (10^{-3} mm^2/s)	D_p (10^{-3} mm^2/s)	CI 95 % (10^{-3} mm^2/s)	f_p (%)	CI 95 % (%)	MVD (MV/mm^2)	CI 95 % (MV/mm^2)
Liver	1.15 ± 0.14	1.10–1.21	50.28 ± 33.21	36.71–65.13	14.77 ± 6.15	12.21–17.54	2008.48 ± 419.43	1921.23–2096.65
Spleen	0.55 ± 0.12	0.50–0.61	24.46 ± 17.31	17.00–32.73	9.89 ± 5.69	7.64–12.47	n.d.	n.d.
Renal medulla	1.50 ± 0.20	1.41–1.60	35.50 ± 18.01	28.66–42.82	14.63 ± 4.07	12.80–16.61	1231.88 ± 290.61	1147.97–1319.78
Renal cortex	1.34 ± 0.18	1.27–1.42	16.74 ± 6.74	14.18–19.65	10.83 ± 3.70	9.35–12.39	810.09 ± 193.50	758.90–860.00
Pancreas	1.23 ± 0.22	1.14–1.34	29.35 ± 17.82	22.05–37.05	20.12 ± 7.46	16.69–23.84	591.15 ± 86.25	566.36–615.30
Bowel	1.06 ± 0.13	1.00–1.12	15.31 ± 7.00	11.73–19.22	16.48 ± 3.63	14.69–18.24	420.50 ± 168.42	372.53–471.46

at 1.23 ± 0.22 × 10^{-3} mm^2/s, liver at 1.15 ± 0.14 x 10^{-3} mm^2/s, and small bowel at 1.06 ± 0.13 × 10^{-3} mm^2/s; the lowest D_t was found in the spleen, at D_t = 0.55 × 10^{-3} mm^2/s.

The mean pseudodiffusion coefficient D_p was highest in the liver, at D_p = 50.28 × 10^{-3} mm^2/s, followed by renal medulla at 35.50 ± 18.01 × 10^{-3} mm^2/s, then pancreas at 29.35 ± 17.82 × 10^{-3} mm^2/s, spleen at 24.46 ± 17.31 × 10^{-3} mm^2/s, and renal cortex at 16.74 ± 6.74 × 10^{-3} mm^2/s, with the lowest D_p being observed in the small bowel, at D_p = 15.31 × 10^{-3} mm^2/s. The measured mean perfusion fraction was detected to be highest for the pancreas, at f_p = 20.12 %, followed by small bowel at 16.48 ± 3.63 %, then liver at 14.77 ± 6.15 %, renal medulla at 14.63 ± 4.07 %, renal cortex at 10.83 ± 3.70 %, and ranged down to f_p = 9.89 % in the spleen. For all retrieved IVIM parameters, parametric maps were computed by voxel-wise fitting and are presented in Fig. 3.

The liver showed the highest MVD of all investigated abdominal organs, at 2008.48 ± 419.43 MV/mm^2, followed by renal medulla at 1231.88 ± 290.61 MV/mm^2, then renal cortex at 810.09 ± 193.50 MV/mm^2, and pancreas at 591.15 ± 86.25 MV/mm^2. The small bowel showed the lowest MVD, at 420.50 ± 168.42, and the MVD could not be determined for the spleen due to cross-reactivities with other cell types in the spleen (see "Discussion"). The PCT and DCT were enumerated, at 346.8 ± 58.2 PCT/mm^2 and 120.4 ± 35.2 DCT/mm^2—again with bootstrapping analysis CI 95 %: 329.7–363.5 PCT/mm^2 and 110.8–131.0 DCT/mm^2. The number of medullary tubules was not determined, as it was not always possible to unambiguously identify the thin and thick segment of the loop of Henle and the collecting duct. Representative images of IHC staining for panendothelial cell antigen CD31 and hematoxylin counterstain used for MVD determination are shown in Fig. 4.

Of the IVIM parameters, D_p (r = 0.90, p = 0.037) correlates significantly with MVD, but no significant correlation could be seen between MVD and D_t (r = 0.40, p = 0.505) or f_p (r = −0.50, p = 0.391) for each of the assessed organs (Fig. 5).

Discussion

In this study, we systematically established the true tissue diffusion coefficient D_t, the pseudodiffusion coefficient D_p, and the perfusion fraction f_p for the liver, spleen, renal cortex and medulla, and pancreas and small bowel on a cohort of C57Bl/6 mice. The retrieved IVIM reference parameters of murine abdominal organs, the described DW-MRI sequence, and the outlined bi-exponential IVIM algorithm allow for future implementation of the IVIM concept into translational research on murine disease models. Further, we provide the MVD as a morphological reference to IVIM parameters.

In recent years, several investigations highlighted the promising applicability of the IVIM concept for lesion characterization in abdominal organs [8–19]. Initial translational research studies using this concept for tissue characterization in the mouse model have thus far been carried out for assessing neoplastic lesions [20, 21], liver fibrosis [26] and placental insufficiency [22]. Furthermore, several well-established murine models of liver diseases (liver fibrosis [27], hepatocellular carcinoma (HCC) [28], nonalcoholic fatty liver disease (NAFLD)/nonalcoholic steatohepatitis (NASH) [29–31]), spleen disorders [32], renal disorders (chronic kidney disease [33], acute kidney injury [34]), pancreatic disorders (pancreatic cancer [35–37], pancreatitis [38]), and inflammatory bowel disease and cancer [39, 40] can be considered for IVIM analysis. Tissue-specific IVIM diffusion parameters reported in this study were thus determined to provide a robust reference for future studies using the outlined murine disease models and to ease transition of IVIM DW-MRI to the human clinical setting for tissue characterization without the need of contrast-enhanced (CE) MRI. As the sensitivity of DW-MRI towards motile water molecules is predefined by the

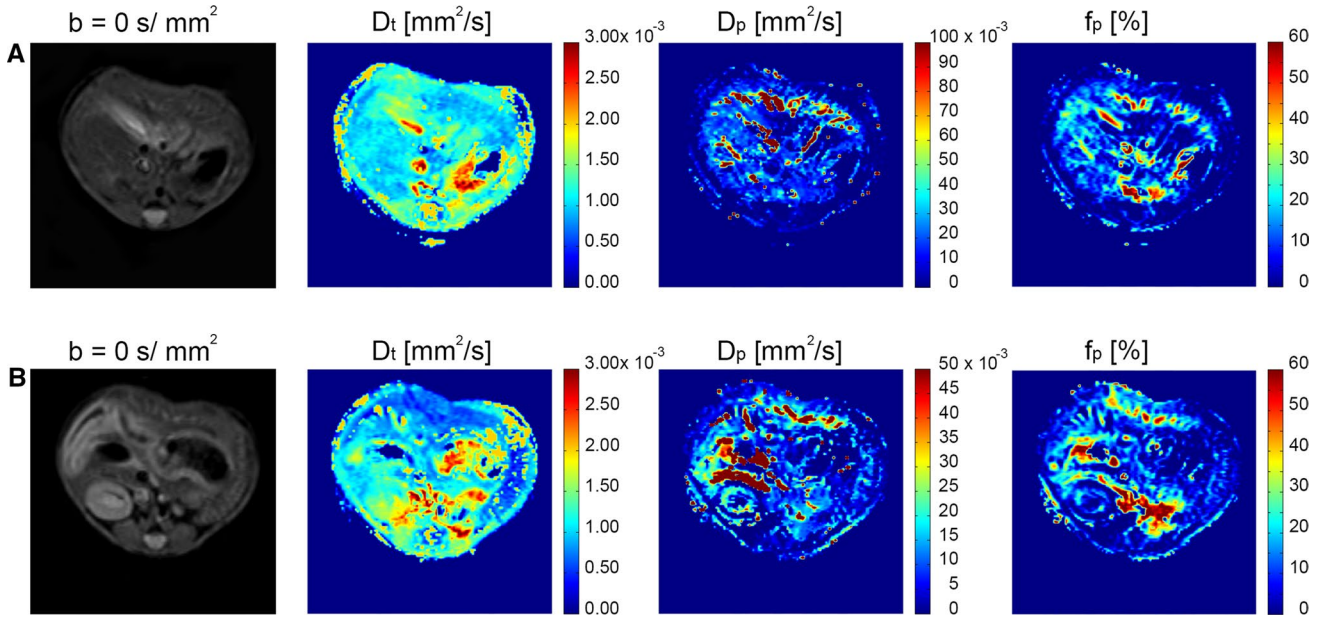

Fig. 3 Upper abdomen (**a**) showing the liver, with proton-density-weighted image acquired at $b = 0$ s/mm^2 and representative parametric maps obtained by voxel-wise fitting of the true tissue diffusion coefficient D_t, pseudodiffusion coefficient D_p, and perfusion fraction f_p. The lower abdomen (**b**), depicting spleen, kidney with renal medulla and renal cortex, pancreas, and small bowel, again with proton-density-weighted image acquired at $b = 0$ s/mm^2 and representative parametric maps obtained by voxel-wise fitting of the true tissue diffusion coefficient D_t, pseudodiffusion coefficient D_p, and perfusion fraction f_p

used b-values containing the amplitude of the two gradient pulses, gradient pulse duration, and elapsed time between applied gradient pulses [41], our systematic approach additionally proves that this set of nine b-values is suitable to reliably quantify the D_t, D_p and f_p values of the mouse abdomen.

The unparalleled strength of the IVIM approach lies in the capability to separate superimposed driving forces of water motion within tissues—namely, diffusion and pseudodiffusion—using bi-exponential fitting of measured signal intensities versus b-values. Water motility in the two investigated processes are reflected by the true tissue diffusion constant D_t and the pseudodiffusion constant D_p. The relative perfusion fraction f_p defines to what extent either process contributes to overall signal attenuation. In this respect, it is noteworthy that most abdominal organs, such as the kidney, liver, and spleen, are highly vascularized tissues [26] and consequently contain not only a higher blood volume but also show an elevated regional blood flow distribution as does the brain, for instance [42]. Blood flow rate of murine liver was determined to be 131 ml/min (20 ml/min hepatic artery and 111 ml/min portal vein contribution), murine kidney 439 ml/min, and murine brain merely 85 ml/min per 100 g tissue [42]. Also in the laboratory mouse, blood volume per wet tissue weight was determined for the brain to be 3 %, liver 36 %, kidney 34 %, small intestine 9 %, and spleen 17 % (v/w) [43]. These data are generally in keeping with another report on the blood volume fraction of laboratory mice, with the brain containing 3.0 %, kidney 24.0 %, liver 31.0 %, and spleen 17.0 % of blood (w/w) [42]. Another study, although performed in the rat, determined the blood volume fraction for the small intestine as 6.3 % (w/w) [44].

The applied IVIM algorithm as well as selection of b-values included into the measurement sequence need to account for the characteristic physiological properties of abdominal organs to disentangle true tissue diffusion and pseudodiffusion. The IVIM-based analysis of the true tissue diffusion coefficient D_t, pseudodiffusion coefficient D_p, and relative perfusion fraction f_p comprises two consecutive algorithms. Considering that D_p is usually significantly greater than D_t, the contribution of pseudodiffusion to the signal decay becomes negligible, with a threshold for b-values $> \sim 1/D_p$ [5]. The simplified monoexponential Eq. (3) allows to deduce D_t and f_p [9, 15], which subsequently enables to infers D_p by a fit with preset D_t and f_p according to Eq. (2). For the brain, this predefined threshold b-value can be set to $b \geq 200$ s/mm^2 for $D_p = 10$ µm^2/ms [8, 45], whereas for the highly vascularized, well perfused abdominal organs, in which expected values were $D_p > 10$ µm^2/ms [26], the effect of perfusion-related water motility becomes insignificant and can be disregarded for $b \geq 100$ s/mm^2, meaning that all signal attenuation beyond the threshold of $b \geq 100$ s/mm^2 is related to true tissue diffusion, and below

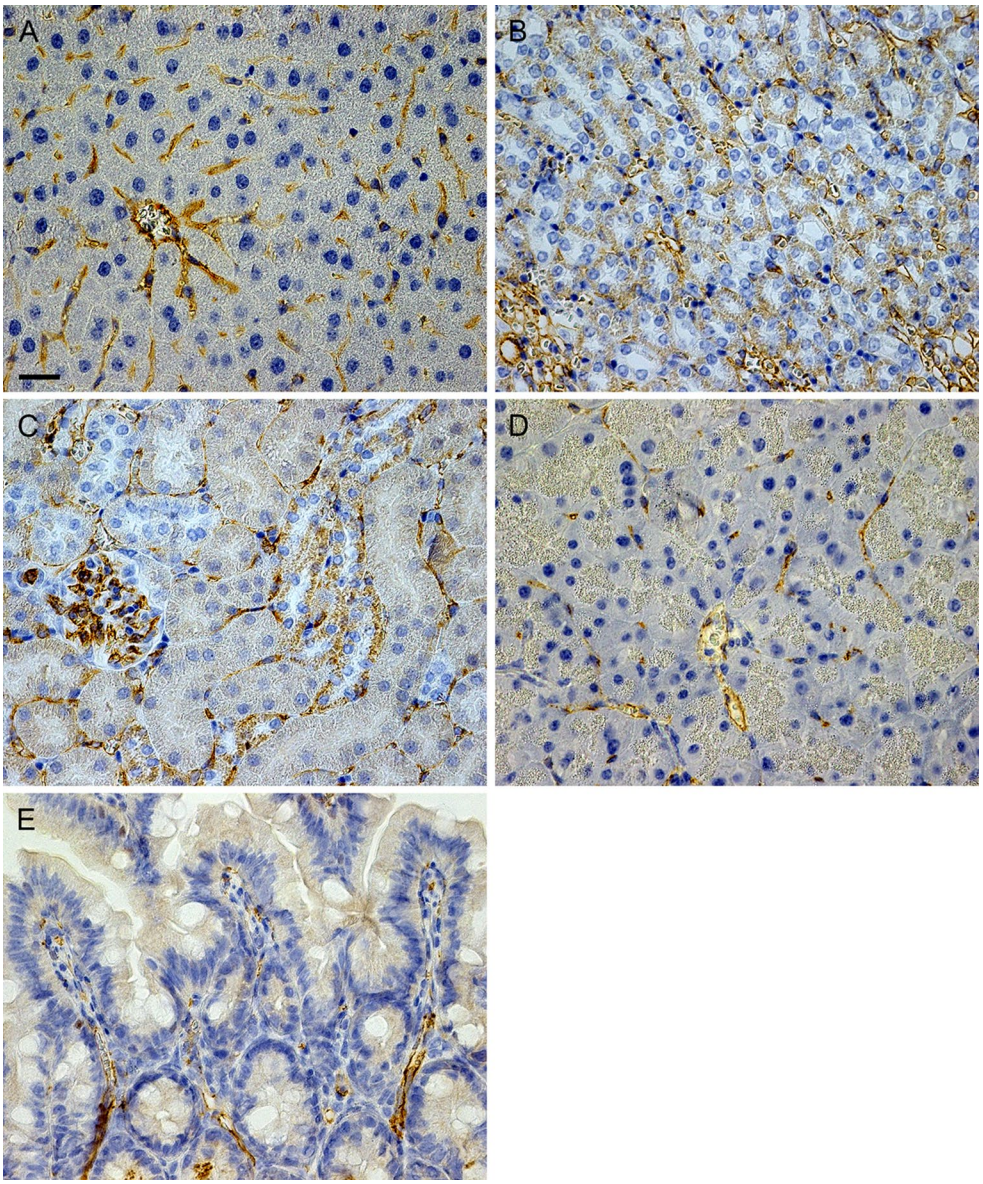

Fig. 4 Representative immunohistochemical images used for microvessel-density (MVD) assessment. Tissues from liver (**a**), renal medulla (**b**), renal cortex (**c**), pancreas (**d**), and small bowel (**e**) were stained for panendothelial cell antigen CD31 and counterstained using hematoxylin. Cells positive for CD31 are indicated by the *dark brown stain* and cell nuclei by *blue*. Tissue sections represent the transversal orientation as displayed on the corresponding IVIM-assessed diffusion-weighted magnetic resonance images. For all images, *scale bar* is 25 μm and *field of view* 0.069 mm^2

the threshold is attributed to both the true diffusion and the pseudodiffussion in accordance with the IVIM model.

A previous IVIM study on healthy and fibrotic mouse liver determined IVIM diffusion parameters on study subjects by using the hepatic pseudodiffusion coefficient $D_p = 27.24 \times 10^{-3}$ mm^2/s [26], thereby using a different set of *b*-values ranging up to $b = 2000$ mm^2/s, with lesser coverage in the lower section of *b*-values (i.e. $b \leq 100$ mm^2/s). This underrepresentation of lower *b*-values might have potentially led to different IVIM diffusion parameters, with a slight underestimation of the pseudodiffusion coefficient. On the contrary, our IVIM parameters demonstrate a generally good agreement, with reported values for the healthy human liver [9, 14]. However, the pseudodiffusion coefficient varies considerably for each IVIM measurement, which was also previously reported in an IVIM study on the human liver [14]. Although individual cell sizes of the mouse liver are about the same as in the human liver, potentially explaining the agreement of the true hepatic tissue diffusion coefficient D_t within

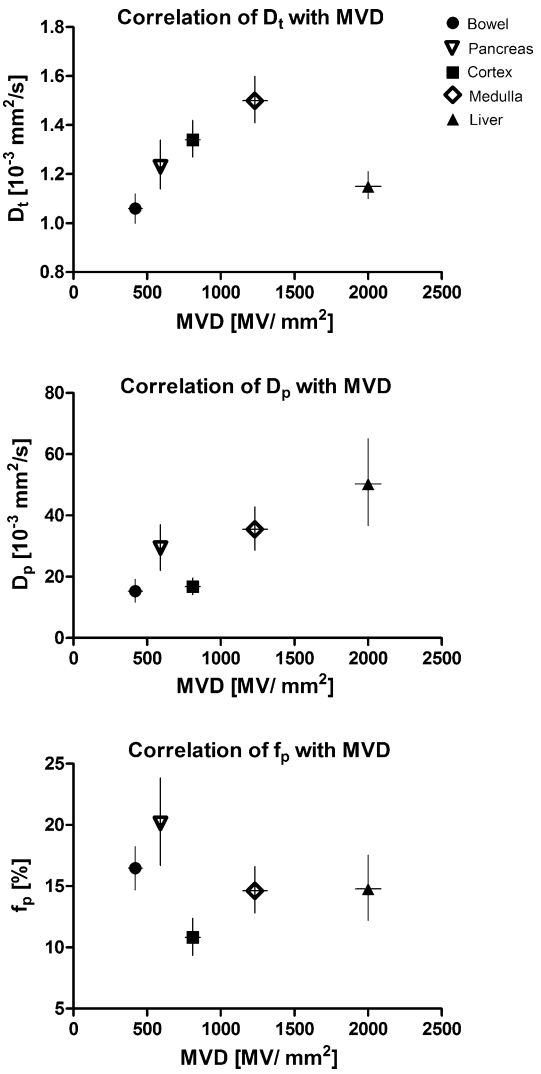

Fig. 5 Correlation between microvessel density (MVD) and true tissue diffusion coefficient D_t, MVD and pseudodiffusion coefficient D_p, and MVD and perfusion fraction f_p for bowel (*filled circle*), pancreas (*inverted triangle*), renal cortex (*filled square*), medulla (*diamond*), and liver (*filled triangle*) and confidence intervals indicated for each intravoxel incoherent motion (IVIM) parameter and the MVD. D_p ; ($r = 0.90$, $p = 0.037$) correlates significantly with MVD for each assessed organ, but no significant correlation could be seen between MVD and D_t ($r = 0.40$, $p = 0.505$) or f_p ($r = -0.50$, $p = 0.391$)

human and mouse, the mouse liver lobule is smaller than the human lobule—the latter having an approximated diameter of up to 1 mm [46]. Assuming, therefore, a mean vessel branch length (l) of the sinusoids, of liver capillaries at 0.45 mm for the human, respectively, at 0.40 mm for the mouse and an average blood velocity (v) of 1 mm/s [21, 47], a pseudodiffusion of $D_p \sim vl/6 \sim 75 \times 10^{-3}$ mm^2/s for the human liver and $D_p \sim 66 \times 10^{-3}$ mm^2/s for the mouse liver can be anticipated and appears to be a plausible D_p value. Nevertheless, another potential factor adding to the observed and reported variability of the liver D_p and f_p values might just be the time of food ingestion, as it has been shown, for instance that postprandial portal vein blood flow increases significantly in rats and humans [48, 49].

The liver is characterized by a relatively high MVD, with ~2000 MV/mm^2. The microcapillaries consist of a single layer of endothelial cells, and the diameter is similar or smaller than red blood cells, which even need to deform in their transit through the capillary [50]. Thus, even single immunoreactive endothelial cells spatially isolated and distinct from other MVs clearly represent an MV. The diffusion distance of oxygen, i.e., the distance from the cell to the nearest capillary in metabolically active tissues, is ~20– 200 µm based on mathematical considerations [51], whereas a rather realistic estimate of the distance oxygen actually can diffuse is 70 µm [52]. Then again, as the liver is perfused by a major proportion of venous blood, an even denser capillary network with intercapillary distances of ~20–25 µm seems to be plausible and corresponds well to an approximated capillary distance observed in a representative image, as shown in Fig. 4.

It is worth mentioning that CD31 as panendothelial cell marker is apparently sensitive to reagents with acidic pH. It was reported that fixatives with acetic acid result in antigen loss [53]. We also observed notable differences between pH 6 versus pH 9 when performing antigen retrieval prior to IHC (data not shown), which is important to consider when comparing different studies applying MVD assessment.

Regarding the spleen, the mean D_t and the mean f_p are considerably low compared with other abdominal organs, although the ROI was placed deliberately outside the fibrous capsule. It is therefore tempting to conjecture that the high abundance of erythrocytes and lymphocytes, with their rather small cell size and consequently reduced intercellular space with increased diffusion restriction, might account for the relatively low observed true splenic diffusion coefficient, which is also reported to be lowest in another abdominal IVIM study performed on humans [54]. The MVD of the spleen could not be determined for several reasons: Although CD31 as a panendothelial cell marker is highly restricted to endothelial cells, it is not absolutely specific; for instance, CD31 is also expressed in myeloid cells [55]. The spleen as a hematopoietic organ in adult mice [56] is therefore prone to cross-reactivity when applying IHC against CD31. Further, splenic sinusoids are neither amenable to IHC with anti-CD34 antibodies, and lymphatic endothelial cells do not reliably stain with anti-von Willebrand factor antibodies [55], which precludes a robust MVD assessment on the spleen.

The kidney is the only anisotropic organ in the abdomen [57]. The IVIM concept assumes a microcirculation of blood within a random network of capillaries, resulting in

such incoherent motions (pseudodiffusion); however, this assumption does not hold entirely true for anisotropically organized structures like the kidney, especially the renal medulla; albeit encouraging IVIM studies have been conducted [15, 16, 58]. In contrast to earlier studies [15, 16], one recent investigation on the human kidney [58] accounts for the almost isotropic environment of the cortex and the strong anisotropic environment of the medulla by a combined IVIM-diffusion tensor imaging (DTI) analysis and reports a clear corticomedullary difference with significantly higher average f_p in the cortex than the medulla.

Our mean f_p values are comparable between cortex and medulla, and the D_p in the medulla is higher than the D_p in the cortex. Both results are in keeping with an earlier investigation on the human kidney [15]. Due to the inherent superposition of vascular flow with tubular flow in the kidney, it was therefore conjectured that a higher tubular flow in the loops of Henle might be responsible for the higher medullary D_p value [15]. As suggested by Le Bihan et al. [59], a reasonable approximation of the occurring blood flow would be represented by the product of D_p, the mean square displacement of water in a given time interval due to perfusion and f_p, the relative perfusion fraction, although under the prerequisite of comparable capillary segment length and total capillary length. Considering our measurements and data of Sigmund et al. [15], the cortical parenchyma would be characterized by less blood flow than the medullary parenchyma, which is not entirely in line with the study of Notohamiprodjo et al. [58]. If there was only vascular flow in the kidney, this finding would seemingly conflict with the fact that the medullary blood flow amounts to only a third of the cortical blood flow in mice [60]. Nevertheless, it is conceivable that IVIM pseudodiffusion measurement of the kidney might be additionally influenced by the distinct hemodynamics of the large volume of glomerular filtrate—or at a later stage of renal reabsorption—by excretable urine, which in turn may potentially compensate to some extent renal hemodynamics of blood flow. Indeed, the glomerular filtration rate of healthy mice was determined with 1.01 ± 0.1 ml/min × g kidney weight [61], and the eventual urine flow was measured as 138.04 µl/min × g kidney weight [60]. The latter study also determined renal blood flow with 7.6 ± 0.5 ml/min × g kidney weight. Therefore, MVD in both the renal cortex and renal medulla might not entirely mirror the measured f_p and D_p values. Hence, we further determined the density of PCT with ~347 ± 58 PCT/mm^2 for the renal cortex, which reportedly possess an average lumen diameter of 23.8 ± 1.2 µm [62], suggesting a remarkable volume of primary filtrate besides actual blood volume. It seems likely, that these two fluid pools—blood and glomerular primary filtrate (respectively urine)—impact on the IVIM perfusion-related f_p and D_p. Therefore, future IVIM studies might be complemented by arterial spin labelling (ASL)-MRI and dynamic contrast-enhanced (DCE)-MRI, additionally to DTI to fully elucidate renal hemodynamics while accounting for structural effects of isotropy/anisotropy [63].

Moreover, major and significant anatomical differences between mouse kidney and human kidney might limit a comparison of our mean renal IVIM diffusion parameters with available human IVIM data sets of the kidney [15, 16, 58]. The mouse kidney is unipyramidal (unilobar), with one renal papilla; in contrast, the human multipyramidal kidney consists of 12–15 cone-shaped renal pyramids with usually seven to nine papilla. Further, the species differ in that mice have greater numbers of long-segment nephrons than short-segment nephrons (3:1), whereas in humans it is vice versa, with a ratio of 7:1 [46]. A previous DW-MRI study on the mouse kidney determined the mean ADC for the renal medulla and renal cortex [64] but lacks additional information about renal water motility provided by the bi-exponential IVIM model.

Although the diagnostic applicability of DW-MRI on the pancreas is controversial [19, 65], a recent DW-MRI patient study implementing the concept of IVIM analysis showed encouraging results for the diagnosis of common pancreatic tumors, also evaluating malignancy of intraductal papillary mucinous neoplasms [18]. The mean human-tissue-specific IVIM parameters of normal pancreas [18] are in keeping with our data, despite the loosely dispersed structure of the mouse pancreas in contrast to the human pancreas, with its rather "compact" presentation and distinct head, neck, body, and tail regions [46]. The determined MVD for the pancreas is relatively low in comparison to the liver. In contrast, the pancreatic f_p value is higher, as the measured liver f_p value—which can be interpreted in that respect, that the pancreatic perfusion contributes proportionally stronger to the general signal attenuation as the pancreatic diffusion does, but again, considering the product, $D_p \times f_p$ as measure of the occurring blood flow, then the liver is much more perfused than the pancreas.

To our knowledge, no IVIM DW-MRI investigation has been carried out on the small bowel of the mouse. Only one IVIM study has staged pediatric Crohn's disease exclusively on patients [66], and one study successfully applied a low *b*-value MRI sequence for diagnosing small-bowel obstruction [67], indicating the need of future IVIM investigations on the bowel. Also, as the perfusion-related f_p and the D_p values suggest, MVD for the small bowel was the lowest of all abdominal organs assessed by IHC.

In this study, we observed that D_p values of the abdominal organs correlate with their MVD, but there was no correlation of D_t and f_p with the MVD for the assessed organs. A previous study reported a correlation of both, the D_p and f_p with the MVD on a mouse tumor model [20]. However, within the morphologically defined region of a tumor, even

more so after the exclusion of necrotic tumors, there is a certain level of tissue homogeneity that, due to the limited size of a tumor, allows for IHC reassessment and subsequent MVD determination on exactly the same region as used initially for the IVIM MRI investigation. In contrast, our study aimed to assess the IVIM parameters of entire organs as reference values and therefore lacks such morphologically distinct and defined regions. Here, the MVD was thus carried out on multiple IHC tissue sections and several randomly selected FoV of each abdominal organ in order to cover the physiological variability within the tissue. Hence, individual IVIM parameters of a certain ROI could not be reliably assigned and correlated to a corresponding area within a histological tissue section.

The observed correlation of D_p, reflecting the motility of water molecules per time interval attributed to perfusion, with the MVD of abdominal organs appears consequential, unlike the relative perfusion fraction f_p, defining the fractional contribution of either water motility—true tissue diffusion or pseudodiffusion—to the observed signal decay, which is also indirectly influenced by diffusion characteristics of the different abdominal organs. Hence, partially reflecting different diffusion properties in the assessed tissues, it is comprehensible that relative perfusion fraction f_p and especially D_t, do not correlate with the MVD across different investigated organs.

In contrast to D_t, with its consistently low SD and narrow CI, D_p and f_p showed higher variability in this investigation, which is also indicated by the parametric maps calculated for D_p and f_p. Respiratory or peristaltic body motion, cardiac pulsation, digestion-related alterations in blood flow to visceral organs [42], and the inherent physiological tissue variability might have contributed to the observed D_p and f_p data variability. Administration of antiperistaltic drugs prior to such IVIM measurements, especially for assessing the lower abdomen, since spleen and bowel were affected by peristalsis in a considerable proportion of the acquired data, and the application of dedicated algorithms for image registration [68, 69], improving image quality and thus the reliability of the retrieved IVIM parameters, might have limited such detrimental effects of peristaltic, respiratory, and cardiac motion. As we did not apply an algorithm for motion compensation, certain slices deteriorated by the outlined artefacts were excluded from further analysis, which represents a limitation of this study.

Moreover, the variability and wider CIs of D_p and f_p might also be a consequence of the applied IVIM approach itself. The IVIM model suggested herein allows the nature of water motility in the parenchyma of several abdominal organs to be assessed at once and to deduce D_t, D_p and f_p values with one IVIM model-fitting algorithm. It is also a limitation that the distribution of *b*-values, especially the determination of the threshold *b*-value discerning pseudodiffusion and true tissue diffusion, were not individually optimized for each of the assessed abdominal organs. This would have resulted in a series of DW-MRI measurements, each dedicated to a certain organ, instead covering all abdominal organs by one measurement. Nevertheless, assuming no perfusion effect beyond the threshold of $b \geq 100$ s/mm^2, as outlined for this IVIM algorithm, might not be optimal for all organs assessed and may have affected the determination of D_t and thus consequentially of f_p and eventually also D_p. Improved parameter estimation techniques proposed in the literature significantly augment the certainty of parameter estimation [70, 71]. Furthermore, as our study was carried out exclusively on mice, it is difficult to assess the impact of technical parameters on IVIM measurement. Additionally, given the time constraints, measurements had to be limited to nine *b*-values, implemented in the DW-MRI sequence, in favor of an improved SNR for the retrieved data sets by acquiring eight signal averages, despite a recent study suggesting a number of at least 10 *b*-values for subsequent IVIM analysis [72]. As there was no disease model in this study, future work is necessary to corroborate the IVIM approach outlined here for use on murine disease models in order to correlate actual pathology to attained diffusion parameters.

Conclusion

In conclusion, this study provides a suitable DW-MRI measurement protocol for a subsequent IVIM analysis allowing a systematic computation of tissue-specific physiological diffusion characteristics on the abdominal organs. Furthermore, the required IVIM reference parameters, true tissue diffusion coefficient D_t, pseudodiffusion coefficient D_p, and perfusion fraction f_p were established on healthy abdominal organs, such as liver, spleen, renal medulla and cortex, pancreas, and small bowel, and the physiological parameter MVD is provided for all organs for future studies on murine disease models.

Acknowledgments The authors gratefully acknowledge the excellent maintenance of the Bruker MRI facility by Udo Ungethuem and the outstanding technical assistance of Ursula Suess, Pia Fuchs and Nadja Bain for the tissue examination by IHC. This study was funded by the Clinical Research Priority Program—Molecular Imaging Network Zurich. ML is supported by a professorship grant from the Swiss National Science Foundation (PP00P3_152990).

Compliance with ethical standards

Ethical approval This animal study was approved by the local veterinary committee (license no. 131/2011) and was therefore performed in accordance with the applicable international, national and institutional guidelines for the care and use of animals.

Conflict of interest The authors declare that they have no conflict of interest.

References

1. Moore WA, Khatri G, Madhuranthakam AJ, Sims RD, Pedrosa I (2014) Added value of diffusion-weighted acquisitions in MRI of the abdomen and pelvis. AJR Am J Roentgenol 202(5):995–1006
2. Schmid-Tannwald C, Oto A, Reiser MF, Zech CJ (2013) Diffusion-weighted MRI of the abdomen: current value in clinical routine. J Magn Reson Imaging 37(1):35–47
3. Chandarana H, Taouli B (2010) Diffusion and perfusion imaging of the liver. Eur J Radiol 76(3):348–358
4. Taouli B, Koh DM (2010) Diffusion-weighted MR imaging of the liver. Radiology 254(1):47–66
5. Le Bihan D, Breton E, Lallemand D, Aubin ML, Vignaud J, Laval-Jeantet M (1988) Separation of diffusion and perfusion in intravoxel incoherent motion MR imaging. Radiology 168(2):497–505
6. Le Bihan D, Breton E, Lallemand D, Grenier P, Cabanis E, Laval-Jeantet M (1986) MR imaging of intravoxel incoherent motions: application to diffusion and perfusion in neurologic disorders. Radiology 161(2):401–407
7. Yamada I, Aung W, Himeno Y, Nakagawa T, Shibuya H (1999) Diffusion coefficients in abdominal organs and hepatic lesions: evaluation with intravoxel incoherent motion echo-planar MR imaging. Radiology 210(3):617–623
8. Le Bihan D (2008) Intravoxel incoherent motion perfusion MR imaging: a wake-up call. Radiology 249(3):748–752
9. Luciani A, Vignaud A, Cavet M, Nhieu JT, Mallat A, Ruel L, Laurent A, Deux JF, Brugieres P, Rahmouni A (2008) Liver cirrhosis: intravoxel incoherent motion MR imaging—pilot study. Radiology 249(3):891–899
10. Yoon JH, Lee JM, Yu MH, Kiefer B, Han JK, Choi BI (2014) Evaluation of hepatic focal lesions usingdiffusion-weighted MR imaging: comparison of apparent diffusion coefficient and intravoxel incoherentmotion-derived parameters. J Magn Reson Imaging 39(2):276–285
11. Chiaradia M, Baranes L, Van Nhieu JT, Vignaud A, Laurent A, Decaens T, Charles-Nelson A, Brugieres P, Katsahian S, Djabbari M, Deux JF, Sobhani I, Karoui M, Rahmouni A, Luciani A (2014) Intravoxel incoherent motion (IVIM) MR imaging of colorectal liver metastases: are we only looking at tumor necrosis? J Magn Reson Imaging 39(2):317–325
12. Ichikawa S, Motosugi U, Ichikawa T, Sano K, Morisaka H, Araki T (2013) Intravoxel incoherent motion imaging of focal hepatic lesions. J Magn Reson Imaging 37(6):1371–1376
13. Doblas S, Wagner M, Leitao HS, Daire JL, Sinkus R, Vilgrain V, Van Beers BE (2013) Determination of malignancy and characterization of hepatic tumor type with diffusion-weighted magnetic resonance imaging: comparison of apparent diffusion coefficient and intravoxel incoherent motion-derived measurements. Invest Radiol 48(10):722–728
14. Andreou A, Koh DM, Collins DJ, Blackledge M, Wallace T, Leach MO, Orton MR (2013) Measurement reproducibility of perfusion fraction and pseudodiffusion coefficient derived by intravoxel incoherent motion diffusion-weighted MR imaging in normal liver and metastases. Eur Radiol 23(2):428–434
15. Sigmund EE, Vivier PH, Sui D, Lamparello NA, Tantillo K, Mikheev A, Rusinek H, Babb JS, Storey P, Lee VS, Chandarana H (2012) Intravoxel incoherent motion and diffusion-tensor imaging in renal tissue under hydration and furosemide flow challenges. Radiology 263(3):758–769
16. Ichikawa S, Motosugi U, Ichikawa T, Sano K, Morisaka H, Araki T (2013) Intravoxel incoherent motion imaging of the kidney: alterations in diffusion and perfusion in patients with renal dysfunction. Magn Reson Imaging 31(3):414–417
17. Rheinheimer S, Stieltjes B, Schneider F, Simon D, Pahernik S, Kauczor HU, Hallscheidt P (2012) Investigation of renal lesions by diffusion-weighted magnetic resonance imaging applying intravoxel incoherent motion-derived parameters—initial experience. Eur J Radiol 81(3):e310–e316
18. Kang KM, Lee JM, Yoon JH, Kiefer B, Han JK, Choi BI (2014) Intravoxel incoherent motion diffusion-weighted MR imaging for characterization of focal pancreatic lesions. Radiology 270(2):444–453
19. Lemke A, Laun FB, Klauss M, Re TJ, Simon D, Delorme S, Schad LR, Stieltjes B (2009) Differentiation of pancreas carcinoma from healthy pancreatic tissue using multiple b-values: comparison of apparent diffusion coefficient and intravoxel incoherent motion derived parameters. Invest Radiol 44(12):769–775
20. Lee HJ, Rha SY, Chung YE, Shim HS, Kim YJ, Hur J, Hong YJ, Choi BW (2014) Tumor perfusion-related parameter of diffusion-weighted magnetic resonance imaging: correlation with histological microvessel density. Magn Reson Med 71(4):1554–1558
21. Kim S, Decarlo L, Cho GY, Jensen JH, Sodickson DK, Moy L, Formenti S, Schneider RJ, Goldberg JD, Sigmund EE (2012) Interstitial fluid pressure correlates with intravoxel incoherent motion imaging metrics in a mouse mammary carcinoma model. NMR Biomed 25(5):787–794
22. Alison M, Chalouhi GE, Autret G, Balvay D, Thiam R, Salomon LJ, Cuenod CA, Clement O, Siauve N (2013) Use of intravoxel incoherent motion MR imaging to assess placental perfusion in a murine model of placental insufficiency. Invest Radiol 48(1):17–23
23. Gudbjartsson H, Patz S (1995) The Rician distribution of noisy MRI data. Magn Reson Med 34(6):910–914
24. Filli L, Boss A, Wurnig MC, Kenkel D, Andreisek G, Guggenberger R (2015) Dynamic intravoxel incoherent motion imaging of skeletal muscle at rest and after exercise. NMR Biomed 28(2):240–246
25. Schneider CA, Rasband WS, Eliceiri KW (2012) NIH image to imagej: 25 years of image analysis. Nat Methods 9(7):671–675
26. Chow AM, Gao DS, Fan SJ, Qiao Z, Lee FY, Yang J, Man K, Wu EX (2012) Liver fibrosis: an intravoxel incoherent motion (IVIM) study. J Magn Reson Imaging 36(1):159–167
27. Weiler-Normann C, Herkel J, Lohse AW (2007) Mouse models of liver fibrosis. Z Gastroenterol 45(1):43–50
28. Heindryckx F, Colle I, Van Vlierberghe H (2009) Experimental mouse models for hepatocellular carcinoma research. Int J Exp Pathol 90(4):367–386
29. Larter CZ, Yeh MM (2008) Animal models of NASH: getting both pathology and metabolic context right. J Gastroenterol Hepatol 23(11):1635–1648
30. Anstee QM, Goldin RD (2006) Mouse models in non-alcoholic fatty liver disease and steatohepatitis research. Int J Exp Pathol 87(1):1–16
31. Takahashi Y, Soejima Y, Fukusato T (2012) Animal models of nonalcoholic fatty liver disease/nonalcoholic steatohepatitis. World J Gastroenterol 18(19):2300–2308
32. Silva TM, Costa EA, Paixao TA, Tsolis RM, Santos RL (2011) Laboratory animal models for brucellosis research. J Biomed Biotechnol 2011:518323
33. Eddy AA, Lopez-Guisa JM, Okamura DM, Yamaguchi I (2012) Investigating mechanisms of chronic kidney disease in mouse models. Pediatric Nephrol Berlin Germany 27(8):1233–1247
34. Wei Q, Dong Z (2012) Mouse model of ischemic acute kidney injury: technical notes and tricks. Am J Physiol Renal Physiol 303(11):F1487–F1494
35. Zhang Y, Chen L, Yang J, Fleming JB, Chiao PJ, Logsdon CD (1835) Li M (2013) Study human pancreatic cancer in mice: how close are they? Biochim Biophys Acta 1:110–118

36. Herreros-Villanueva M, Hijona E, Cosme A, Bujanda L (2012) Mouse models of pancreatic cancer. World J Gastroenterol 18(12):1286–1294
37. Guerra C, Barbacid M (2013) Genetically engineered mouse models of pancreatic adenocarcinoma. Mol Oncol 7(2):232–247
38. Hyun JJ, Lee HS (2014) Experimental models of pancreatitis. Clin Endosc 47(3):212–216
39. Fox JG, Ge Z, Whary MT, Erdman SE, Horwitz BH (2011) Helicobacter hepaticus infection in mice: models for understanding lower bowel inflammation and cancer. Mucosal Immunol 4(1):22–30
40. Jones-Hall YL, Grisham MB (2014) Immunopathological characterization of selected mouse models of inflammatory bowel disease: comparison to human disease. Pathophysiology: the official journal of the International Society for Pathophysiology/ISP
41. Bammer R (2003) Basic principles of diffusion-weighted imaging. Eur J Radiol 45(3):169–184
42. Brown RP, Delp MD, Lindstedt SL, Rhomberg LR, Beliles RP (1997) Physiological parameter values for physiologically based pharmacokinetic models. Toxicol Ind Health 13(4):407–484
43. Kaliss N, Pressman D (1950) Plasma and blood volumes of mouse organs, as determined with radioactive iodoproteins. Proceedings of the Society for Experimental Biology and Medicine Society for Experimental Biology and Medicine (New York, NY) 75 (1):16–20
44. Triplett JW, Hayden TL, McWhorter LK, Gautam SR, Kim EE, Bourne DW (1985) Determination of gallium concentration in "blood-free" tissues using a radiolabeled blood marker. J Pharm Sci 74(9):1007–1009
45. Le Bihan D (2012) Diffusion, confusion and functional MRI. NeuroImage 62(2):1131–1136
46. Treuting PM, Dintzis SM, Frevert CW, Montine KS (2012) Comparative anatomy and histology: a mouse and human atlas. Elsevier/Academic Press, Amsterdam
47. Nevo U, Ozarslan E, Komlosh ME, Koay CG, Sarlls JE, Basser PJ (2010) A system and mathematical framework to model shear flow effects in biomedical DW-imaging and spectroscopy. NMR Biomed 23(7):734–744
48. Delp MD, Manning RO, Bruckner JV, Armstrong RB (1991) Distribution of cardiac output during diurnal changes of activity in rats. Am J Physiol 261(5 Pt 2):H1487–H1493
49. Okazaki K, Miyazaki M, Onishi S, Ito K (1986) Effects of food intake and various extrinsic hormones on portal blood flow in patients with liver cirrhosis demonstrated by pulsed Doppler with the Octoson. Scand J Gastroenterol 21(9):1029–1038
50. Kim HW, Greenburg AG (2013) Hemoglobin-based oxygen carriers as red cell substitutes and oxygen therapeutics. Springer, Berlin Heidelberg
51. Tuma RF, Durán WN, Ley K (2008) Microcirculation. Elsevier/Academic Press, Amsterdam
52. Hall EJ, Giaccia AJ (2006) Radiobiology for the Radiologist. Williams & Wilkins, Lippincott
53. Nico B, Benagiano V, Mangieri D, Maruotti N, Vacca A, Ribatti D (2008) Evaluation of microvascular density in tumors: pro and contra. Histol Histopathol 23(5):601–607
54. Jerome NP, Orton MR, d'Arcy JA, Collins DJ, Koh DM, Leach MO (2014) Comparison of free-breathing with navigator-controlled acquisition regimes in abdominal diffusion-weighted magnetic resonance images: effect on ADC and IVIM statistics. J Magn Reson Imaging 39(1):235–240
55. Ordonez NG (2012) Immunohistochemical endothelial markers: a review. Adv Anat Pathol 19(5):281–295
56. Morita Y, Iseki A, Okamura S, Suzuki S, Nakauchi H, Ema H (2011) Functional characterization of hematopoietic stem cells in the spleen. Exp Hematol 39(3):351–359 e353
57. Roy C, Matau A, Bierry G, Bazille G (2010) Diffusion-weighted MR imaging of the kidney. J Radiol 91(3 Pt 2):408–418
58. Notohamiprodjo M, Chandarana H, Mikheev A, Rusinek H, Grinstead J, Feiweier T, Raya JG, Lee VS, Sigmund EE (2015) Combined intravoxel incoherent motion and diffusion tensor imaging of renal diffusion and flow anisotropy. Magn Reson Med 73(4):1526–1532
59. Le Bihan D, Turner R (1992) The capillary network: a link between IVIM and classical perfusion. Magn Reson Med 27(1):171–178
60. Gross V, Lippoldt A, Bohlender J, Bader M, Hansson A, Luft FC (1998) Cortical and medullary hemodynamics in deoxycorticosterone acetate-salt hypertensive mice. J Am Soc Nephrol JASN 9(3):346–354
61. Cervenka L, Mitchell KD, Navar LG (1999) Renal function in mice: effects of volume expansion and angiotensin II. J Am Soc Nephrol JASN 10(12):2631–2636
62. Bordier B, Ornstein L, Weeden RP (1970) The intrarenal distribution of tritiated para-aminohippuric acid determined by a modified technique of section freeze-dry radioautography. J Cell Biol 46(3):518–532
63. Zhang JL, Rusinek H, Chandarana H, Lee VS (2013) Functional MRI of the kidneys. J Magn Reson Imaging 37(2):282–293
64. Hueper K, Rong S, Gutberlet M, Hartung D, Mengel M, Lu X, Haller H, Wacker F, Meier M, Gueler F (2013) T2 relaxation time and apparent diffusion coefficient for noninvasive assessment of renal pathology after acute kidney injury in mice: comparison with histopathology. Invest Radiol 48(12):834–842
65. Sandrasegaran K (2014) Functional MR imaging of the abdomen. Radiol Clin North Am 52(4):883–903
66. Freiman M, Perez-Rossello JM, Callahan MJ, Bittman M, Mulkern RV, Bousvaros A, Warfield SK (2013) Characterization of fast and slow diffusion from diffusion-weighted MRI of pediatric Crohn's disease. J Magn Reson Imaging 37(1):156–163
67. Takahara T, Kwee TC, Sadahiro S, Yamashita T, Toyoguchi Y, Yoshizako T, Horie T, Luijten PR, Imai Y (2011) Low b-value diffusion-weighted imaging for diagnosing strangulated small bowel obstruction: a feasibility study. J Magn Reson Imaging 34(5):1117–1124
68. Kurugol S, Freiman M, Afacan O, Domachevsky L, Perez-Rossello JM, Callahan MJ, Warfield SK (2015) Motion compensated abdominal diffusion weighted MRI by simultaneous image registration and model estimation (SIR-ME). Med Image Comput Comput Assist Interv MICCAI Int Conf Med Image Comput Comput Assist Interv 9351:501–509
69. Guyader JM, Bernardin L, Douglas NH, Poot DH, Niessen WJ, Klein S (2015) Influence of image registration on apparent diffusion coefficient images computed from free-breathing diffusion MR images of the abdomen. J Magn Reson Imaging 42(2):315–330
70. Freiman M, Perez-Rossello JM, Callahan MJ, Voss SD, Ecklund K, Mulkern RV, Warfield SK (2013) Reliable estimation of incoherent motion parametric maps from diffusion-weighted MRI using fusion bootstrap moves. Med Image Anal 17(3):325–336
71. Wurnig MC, Donati OF, Ulbrich E, Filli L, Kenkel D, Thoeny HC, Boss A (2015) Systematic analysis of the intravoxel incoherent motion threshold separating perfusion and diffusion effects: proposal of a standardized algorithm. Magn Reson Med 74(5):1414–1422
72. Lemke A, Stieltjes B, Schad LR, Laun FB (2011) Toward an optimal distribution of b values for intravoxel incoherent motion imaging. Magn Reson Imaging 29(6):766–776